Modelling the development and decay of cryoconite holes in Northwest Greenland

Yukihiko Onuma[1], Koji Fujita[2], Nozomu Takeuchi[3], Masashi Niwano[4] and Teruo Aoki[5]

[1]Earth Observation Research Center (EORC), Japan Aerospace Exploration Agency (JAXA), Tsukuba, 305-8505, Japan
5 [2]Graduate School of Environmental Studies, Nagoya University, Nagoya 464-8601, Japan
[3]Graduate School of Science, Chiba University, Chiba 263-8522, Japan
[4]Meteorological Research Institute, Japan Meteorological Agency, Tsukuba 305-0052, Japan
[5]National Institute of Polar Research, Tokyo 190-8518, Japan

10 *Correspondence to*: Yukihiko Onuma[1] and Koji Fujita[2] ([1]onuma.yukihiko@jaxa.jp and [2]cozy@nagoya-u.jp)

Abstract. Cryoconite holes (CHs) are water-filled cylindrical holes with cryoconite (dark-coloured sediment) deposited at their bottoms, forming on ablating ice surfaces of glaciers and ice sheets worldwide. Because the collapse of CHs may disperse cryoconite on the ice surface, thereby decreasing the ice surface albedo, accurate simulation of the temporal changes in CH depth is essential for understanding ice surface melt. We established a novel model that simulates the temporal changes in CH
15 depth using heat budgets calculated independently at the ice surface and CH bottom based on hole-shape geometry. We evaluated the model with in situ observations of the CH depths on the Qaanaaq ice cap in Northwest Greenland during the 2012, 2014, and 2017 melt seasons. The model reproduced well the observed depth changes and timing of CH collapse. Although earlier models have shown that CH depth tends to be deeper when downward shortwave radiation is intense, our sensitivity tests suggest that deeper CH tends to form when the diffuse component of downward shortwave radiation is
20 dominant, whereas CHs tend to be shallower when the direct component is dominant. In addition, the total heat flux to the CH bottom is dominated by shortwave radiation transmitted through ice rather than that directly from the CH mouths when the CH is deeper than 10 mm. Furthermore, the tests highlight that the ice surface albedo is a key parameter for accurately reproducing the timing of CH collapse because 0.1 decrease in albedo induces the CH collapse one day earlier. Heat component analysis suggests that CH depth is governed by the balance between the intensity of the diffuse component of downward
25 shortwave radiation and the wind speed. Therefore, these meteorological conditions may be important factors contributing to the recent surface darkening of the Greenland ice sheet and other glaciers via the redistribution of CHs. Coupling the CH model proposed in this study with a climate model should improve our understanding of glacier-surface darkening.

1. Introduction

Cryoconite holes (CHs), cylindrical water-filled holes formed on ablating ice surfaces of glaciers and ice sheets worldwide,
30 influence the ablation process of glacial ice and function as the habitats of glacial microbes (e.g., Hodson et al., 2010a; Cook et al., 2016; Uetake et al., 2016; Zawierucha et al., 2021). In CHs, dark-coloured sediment, referred to as cryoconite, is

deposited at the bottoms; it consists mostly of spherical aggregates (cryoconite granules) formed by the entanglement of filamentous cyanobacteria with mineral and organic particles (Hodson et al., 2010b; Langford et al., 2010; Takeuchi et al., 2010, 2014; Wientjes et al., 2011; Uetake et al., 2019). Because such dark-coloured sediment on bare ice absorbs solar radiation
35 more effectively than the surrounding clear ice, CH formation occurs often.

The development and decay of CHs depend on the meteorological conditions near the ice surface. CHs are likely to form well under sunny conditions (McIntyre, 1984; Fountain et al., 2008; Jepsen et al., 2010; Cook et al., 2016; Takeuchi et al., 2018). Although many studies have investigated which meteorological conditions are favourable for the deepening (development) of CHs, there is limited information on their shallowing (decay) dynamics. Takeuchi et al. (2018) reported that
40 CHs collapse under cloudy and windy conditions in summer in Northwest Greenland. They suggested that CHs collapse when the ice surface surrounding the CHs experiences enhanced melt caused by turbulent heat flux exchange. CH collapse events have also been reported in Svalbard (Hodson et al., 2007, 2008; Stibal et al., 2008; Irvine-Fynn et al., 2011), while it has been indicated that a higher melt rate at the ice surface induces CH collapse (Hodson et al., 2007).

The development and decay of CHs modulate the ice surface albedo. On the one hand, the development of CHs increases
45 the area-averaged ice surface albedo compared to the case where the surface is uniformly covered with cryoconite granules, because cryoconite granules in holes are shielded from sunlight by the hole walls (Bøggild et al., 2010; Takeuchi et al., 2014; Chandler et al., 2015). On the other hand, the collapse of CHs reduces the area-average surface albedo by approximately 0.1–0.2 due to the redistributed cryoconite on the ice surface (Irvine-Fynn et al., 2011; Takeuchi et al., 2018). Topologically heterogeneous ice surfaces can be classified into three types: bare ice surfaces, surfaces with CHs, and meltwater streams
50 (Irvine-Fynn and Edwards, 2014; Holland et al., 2019; Tedstone et al., 2020). Bare ice surfaces and surfaces with CHs are estimated to account for approximately 80–90 and 5–15 %, respectively, of the ablation area of the southwestern Greenland ice sheet (GrIS) (Chandler et al., 2015). Therefore, both the development and decay of CHs are important for the surface albedo dynamics of the GrIS.

Numerical models have been used for reproducing the temporal changes in CH depth; however, only few models consider
55 the decay of CHs. Gribbon (1979) proposed a conceptual model based on the Beer–Lambert law to simulate the development of CHs. By using solar radiation and CH depth, this model calculates the shortwave radiation reaching the cryoconite at the CH bottoms using the absorption coefficient of ice. Although several studies have proposed numerical models following Gribbon (Podgorny and Grenfell, 1996; Jepsen et al., 2010; Cook, 2012), these models focus only on the development of CHs. Therefore, to reproduce CH decay processes, such as CH collapse events, a model that simulates melt not only at the CH
60 bottom, but also at the ice surface surrounding the CHs is necessary.

In this study, we established a numerical model to simulate the temporal changes in CH depth, accounting for both the development and decay of CHs, based on a concept different from those in previous studies [e.g., Gribbon (1979)]. We evaluated the model using observed temporal changes in CH depth from the Qaanaaq ice cap in Northwest Greenland. We further performed numerical model sensitivity analyses to reveal how the CH depth is controlled by the meteorological

65   variables, hole geometry, albedos of the ice surface surrounding the CHs and the cryoconite therein, and optical parameters of
ice. Finally, we assessed the meteorological factors controlling the CH depth changes based on heat component analysis.

2. Cryoconite hole model (CryHo)

The cryoconite hole model (hereafter referred to as CryHo) developed in this study calculates the heat balances and resultant
melt rates at the ice surface and CH bottom independently (Fig. 1). All variables and constants described in the following
70   equations are listed in Table 1.

2.1. Heat balance at the ice surface

The heat balance at the ice surface (Q_i, W m^{-2}) is described as follows:

$$Q_i = (1 - \alpha_i)R_S + R_{Lni} + H_{Si} + H_{Li}, \tag{1}$$

$$R_{Lni} = \varepsilon R_L - \varepsilon \sigma (T_i + 273.15)^4, \tag{2}$$

75   where α_i is the ice surface albedo (dimensionless), R_S is the downward shortwave radiation (W m^{-2}), R_{Lni} is the net longwave
radiation (W m^{-2}), H_{Si} is the sensible heat flux (W m^{-2}), H_{Li} is the latent heat flux (W m^{-2}), ε is the emissivity of the snow/ice
surface, which is assumed to be 1.0 (dimensionless), R_L is the downward longwave radiation (W m^{-2}), σ is the Stefan–
Boltzmann constant (5.67×10^{-8} W m^{-2} K^{-4}), and T_i is the surface temperature (°C). Subscript i used in the variables refers to
the ice surface. All the downward components have positive signs. Heat conduction from/toward the glacier ice and heat
80   supplied by rainwater are assumed to be negligible. The turbulent heat fluxes (i.e., H_{Si} and H_{Li}) were estimated using the
following bulk formulations:

$$H_{Si} = c_P \rho_a CU(T_a - T_i), \tag{3}$$

$$H_{Li} = l_E \rho_a CU\big(h_r q(T_a) - q(T_i)\big), \tag{4}$$

where c_P is the specific heat of air (1,006 J K^{-1} kg^{-1}), ρ_a is the air density (kg m^{-3}), C is the bulk coefficient for the snow/ice
85   surface (0.0025), U is the wind speed (m s^{-1}), T_a is the air temperature (°C), l_E is the latent heat of water evaporation ($2.50 \times$
10^6 J kg^{-1}), h_r is the relative humidity (dimensionless), and $q(T)$ is the saturated specific humidity (kg kg^{-1}). The excess energy
($Q_i > 0$) is used to melt the ice at the surface, once the surface temperature reaches 0 °C, and its hourly amount is obtained as
follows:

$$Q_{Mi} = \max[0, Q_i], \tag{5}$$

$$M_i = \frac{t_h Q_{Mi}}{l_M},$$

90

where Q_{Mi} is the excess heat energy for ice melt (W m^{-2}), M_i is the hourly amount of ice melt (mm w. e. h^{-1}), t_h is the length of an hour in seconds (3,600 s), and l_M is the latent heat of ice melt (3.33×10^5 J kg^{-1}).

2.2. Heat balance at the cryoconite hole bottom

The heat balance and melt rate at the CH bottom (denoted by subscript c) are defined as follows:

95

$$Q_c = (1 - \alpha_c)(R_{Sdc} + R_{Sfc} + R_{Stdc} + R_{Stfc}) + R_{Lnc}, \tag{6}$$

$$Q_{Mc} = \max[0, Q_c], \tag{7}$$

$$M_c = \frac{t_h Q_{Mc}}{l_M},$$

where Q_c is the heat balance at the bottom (W m^{-2}); α_c is the albedo (dimensionless); R_{Sdc} and R_{Sfc} are the direct and diffuse components of shortwave radiation (W m^{-2}); R_{Stdc} and R_{Stfc} are the direct and diffuse components of shortwave radiation transmitted through ice (W m^{-2}); R_{Lnc} is the net longwave radiation (W m^{-2}); Q_{Mc} is the excess heat energy for ice melt (W m^{-2}); and M_c is the hourly amount of ice melt (mm w. e. h^{-1}). Because we assume that the CH is filled with water (not fully, but partially), the turbulent heat fluxes at the bottom of the CH (i.e., H_{Sc} and H_{Lc}) are assumed to be zero in Eq. (6). The change in CH depth (D_t, mm) at a given time (t) is defined as follows:

$$D_t = D_{t-1} + (M_c - M_i)\frac{\rho_w}{\rho_i}, \tag{8}$$

105

where D_{t-1} is the CH depth at one time step before (mm), and ρ_i and ρ_w are the ice and water densities assumed equal to 900 and 1,000 kg m^{-3}, respectively. If the melt rate at the CH bottom is greater than that at the ice surface ($M_c > M_i$), the CH depth deepens, and vice versa. The initial depth D_0 at $t = 0$ in CryHo is a prescribed constant initial condition.

2.3. Geometry effect on the radiation components

In earlier CH models (Gribbon, 1979; Jepsen et al., 2010; Cook, 2012), downward shortwave radiation is reduced exponentially with increasing CH depth. The novel aspect of our model is that it considers not only the CH depth, but also the CH shape geometry. The direct and diffuse components of downward shortwave radiation and downward longwave radiation

are also considered independently. Regarding downward shortwave radiation, we first distinguish the observed downward shortwave radiation into direct and diffuse components (R_{Sd} and R_{Sf}, W m^{-2}) as follows:

$$R_{Sd} = (1 - r_{dif})R_S, \tag{9}$$
$$R_{Sf} = r_{dif}R_S, \tag{10}$$

115

where r_{dif} is the diffuse ratio of downward shortwave radiation (dimensionless; 0–1), which is calculated following Goudriaan (1977):

$$r_{dif} = r_{ze} + (1 - r_{ze})r_{cld}, \tag{11}$$

120 where r_{ze} is the ratio based on the zenith angle (dimensionless; 0–1); and r_{cld} is the ratio based on cloudiness (dimensionless; 0–1). Calculations of r_{ze} and r_{cld} were performed following Goudriaan (1977) and Niwano et al. (2015), respectively:

$$r_{ze} = \frac{0.0604}{\max[0.01, (\cos\theta_z - 0.0223)]} + 0.0683, \tag{12}$$
$$r_{cld} = 1 - \frac{R_{Lni}}{[1363.2 - 5.4(T_a + 273.15)]}, \tag{13}$$

where θ_z is the solar zenith angle (radian).

125 The CH geometry is defined as the zenith angle of the edge from the centre of the CH bottom (θ_c, rad) as follows:

$$\theta_c = \tan^{-1}\left(\frac{\phi}{2D_{t-1}}\right), \tag{14}$$

where ϕ is the diameter of CH (mm).

Compared with the solar zenith angle, the direct component of shortwave radiation from the sky looking up from the CH 130 bottom (R_{Sdc}; W m^{-2}) is calculated as follows:

$$R_{Sdc} = R_{Sd} \quad [if\ \theta_z \le \theta_c], \tag{15}$$
$$R_{Sdc} = 0 \quad\quad [if\ \theta_z > \theta_c].$$

Meanwhile, the diffuse component of shortwave radiation from the sky looking up from the CH bottom (R_{Sfc}, W m^{-2}) is obtained as follows:

135

$$R_{Sfc} = (1 - \cos^2 \theta_c) R_{Sf}. \tag{16}$$

Shortwave radiation components transmitted through ice are described in the following section.

Longwave radiation from the sky looking up from the CH bottom (R_{Lc}; W m^{-2}) can be obtained in a manner similar to R_{Sfc} as follows:

140

$$R_{Lc} = (1 - \cos^2 \theta_c) \varepsilon R_L. \tag{17}$$

Longwave radiation from the CH wall (R_{Lw}; W m^{-2}) is subsequently described as follows:

$$R_{Lw} = \cos^2 \theta_c \, \varepsilon \sigma (T_i + 273.15)^4. \tag{18}$$

145 Here, we assume that the CH bottom temperature is equal to the surface temperature. Regarding longwave radiation emitted from the CH bottom, the net longwave radiation (R_{Lnc}; W m^{-2}) can be summarised as follows:

$$R_{Lnc} = R_{Lc} + R_{Lw} - \varepsilon \sigma (T_i + 273.15)^4 = (1 - \cos^2 \theta_c) R_{Lni}. \tag{19}$$

2.4. Shortwave radiation transmitted through ice

150 Depending on whether direct solar radiation illuminates the CH bottom ($\theta_z \leq \theta_c$) or not ($\theta_z > \theta_c$), the direct and diffuse components of shortwave radiation transmitted through the ice (R_{Stdc} and R_{Stfc}, W m^{-2}) are described as follows:

$$R_{Stdc} = e^{\frac{-\kappa_d D_{t-1}}{1000 \cos \theta_0}} R_{Sd} \quad [if \ \theta_z > \theta_c], \tag{20}$$
$$R_{Stdc} = 0 \quad\quad\quad\quad [if \ \theta_z \leq \theta_c],$$
$$R_{Stfc} = \cos^2 \theta_c \, e^{\frac{-\kappa_f D_{t-1}}{1000}} R_{Sf}, \tag{21}$$

where κ_d and κ_f are the broadband asymptotic volume flux extinction coefficients (hereinafter broadband flux extinction

155 coefficients) of ice (m^{-1}) for the direct and diffuse components, respectively. For the direct component, the pass length of the

transmitted light is considered, whereas for the diffuse component, it is assumed to be the CH depth. The units of D_{t-1} (mm) in equations (20) and (21) are converted to meters by diving with 1,000.

    The broadband flux extinction coefficient for the diffuse component (κ_f) can be calculated from the spectral flux extinction coefficients; however, this is not a simple integration because the spectral distribution of shortwave radiation transmitted through the ice varies depending on both the spectral distribution of solar illumination and the path length in the ice. Thus, we first calculate the spectral distribution of insolation in the ice from both the spectral flux extinction coefficients experimentally determined by Cooper et al. (2021) for ice on the GrIS (the term "irradiance attenuation coefficient" was used in their study) and the spectral solar radiation at the ice surface assumed for clear and cloudy skies, computed using a radiative transfer model (Aoki et al., 1999; 2000). From these parameters, the spectrally integrated flux transmittance is calculated and transformed into broadband flux extinction coefficients, which are tested for their dependence on solar zenith angle, cloudiness, and ice thickness (see Fig. S1). The details of the deviation in the broadband flux extinction coefficient are presented in the supplementary text. Finally, we determine the following approximation equations of the broadband flux extinction coefficients as a function of ice thickness for clear (κ_{clr}; m^{-1}) and cloudy (κ_{cld}; m^{-1}) skies (Eq. S4 and Fig. S4).

$$\kappa_{clr} = 1.9167 \left(\frac{D_{t-1}}{1000}\right)^{-0.61328}, \tag{22}$$

$$\kappa_{cld} = 1.6203 \left(\frac{D_{t-1}}{1000}\right)^{-0.51923}. \tag{23}$$

The broadband flux extinction coefficient for the diffuse component (κ_f) is determined in a similar manner for the estimation of R_{Sfd} and R_{Sfs} as follows:

$$\kappa_f = (1 - r_{dif})\kappa_{clr} + r_{dif}\kappa_{cld}. \tag{24}$$

As there are no available data for estimating the extinction coefficient for the direct component (κ_d), we parameterize it by introducing a coefficient (r_d) as follows:

$$\kappa_d = r_d \kappa_f. \tag{25}$$

The coefficient r_d was assumed to be 1.0, and the effect of this assumption was later tested.

3. Observations

3.1. Site location

To evaluate the model, we investigated changes in CH depth at the Qaanaaq ice cap in Northwest Greenland (Fig. 2) during the 2012, 2014, and 2017 summer seasons. The ice cap covers an area of 286 km² and has an elevation range of 0–1,200 m a.s.l. (Sugiyama et al, 2014). We selected five study sites at different elevations (Sites 1 to 5) on the Qaanaaq Glacier, which is an outlet glacier of the ice cap that is easily accessible from Qaanaaq Village. Sites 1 to 5 are located in the middle of the glacier at elevations of 247, 441, 672, 772 and 944 m a.s.l., respectively. The equilibrium line elevation of the glacier ranged between 862 and 1,001 m a.s.l. in early August 2012, 2014, and 2017 (Tsutaki et al., 2017); hence, the ice surfaces at Sites 1 to 5 were exposed during the ablation period from July to August.

3.2. Observations of meteorological variables and surface reflectance

The meteorological data that were used as input in CryHo were collected with an automatic weather station (AWS), which was established at the SIGMA-B site (77.518° N, 69.0619° W; 944 m a.s.l.), i.e., at Site 5 in this study, on 19 July 2012 (Aoki et al., 2014; Nishimura et al., 2021). Hourly air temperature (T_a; °C), relative humidity (h_r; dimensionless), downward shortwave radiation (R_S; W m⁻²), downward longwave radiation (R_L; W m⁻²), upward longwave radiation (R_{Lui}; W m⁻²), wind speed (U; m s⁻¹), and air pressure (P_a; hPa) were collected for the model simulations described in Sect. 4. The seasonal changes of the measured air and surface temperatures and the calculated daily surface energy balance during the three studied summer seasons are shown in Fig. 3. The air and surface temperatures support the assumption that all study sites below the SIGMA-B site (i.e., Site 5) were mostly in ablation conditions during the three studied summer seasons. The heat balance was similar across the study years.

To determine the ice surface albedo used as input in CryHo, we measured the spectral reflectance from the visible to near-infrared band (0.350–1.050 μm) on the ice surface using a spectrometer (MS-720, Eiko Seiki Co., Japan) at the study sites during the 2014 and 2017 summer seasons (Table 2). For details on the observation method, we refer to Takeuchi et al. (2015). Although the mean reflectance differs optically from broadband albedo (0.300–3.000 μm), the reflectance measured at Site 3 in 2014 agrees well with the broadband albedo at the same site measured in 2012 (0.4 versus approximately 0.4; Takeuchi et al., 2018). Therefore, we assume that the reflectance shown in Table 2 can be used as a proxy for broadband albedo at the study sites for numerical simulations.

3.3. Monitoring cryoconite hole depth

To collect in situ data that can be used for the evaluation of CryHo, the temporal changes in CH depth were observed using the monitoring device, which consisted of two time-lapse cameras as well as a plastic stick positioned in the centre of a CH, supported by metal angles (Fig. 4a). The temporal changes in CH depth were derived from variations in the heights of the plastic stick and white metal angle (Figs 4b–d). To measure the variations, we marked both the stick and angle with clear and

black colours at 5 cm intervals. The stick and angle were used to estimate the melt rates at the CH bottoms and ice surface
surrounding the CHs, respectively. The variations were measured from hourly images with a resolution of $4{,}608 \times 2{,}592$ pixels
captured by a time-lapse camera (PENTAX WG-10, RICOH Co., Japan) installed at 3 m from the marked stick and angle. The
time-lapse camera was placed 1 m above the ice surface, while being orthogonally oriented to the ice surface. To maintain the
215   camera at the same height from the ice surface, we adjusted the height regularly (i.e., every 5–10 days). To capture the CH
collapse event and check whether the plastic stick remained positioned in the CH, we also monitored the CHs using hourly
images with a resolution of 1280×1022 pixels taken by another time-lapse camera (GardenWatch Cam, Brinno Co., Taiwan,
Fig. 4b). The location of the device was selected to have a suite of characteristics broadly identical to those of the monitoring
site in a previous study (Takeuchi et al., 2018) in terms of cryoconite loading, ice structure, and ice surface slope of ~5°.
220   Monitoring was conducted from day of the year (DOY) 194 to 214 in 2014.

     To estimate the CH depths, the images were processed using ImageJ (version 1.48, National Institutes of Health, USA;
Schneider et al., 2012). The CH depths were measured as relative variations using the length of marks on the stick for the CH
bottom (Fig. 4c) and on the angle for the ice surface (Fig. 4d). One pixel corresponds to approximately 1 mm. Because the
monitored CH collapsed between DOY 202 and 204, the stick and angles were reinstalled into another CH on DOY 205 (Fig.
225   4e).

     Camera-based observations were conducted at Site 2, near the site where CH collapse occurred in 2012 (Takeuchi et al.,
2018). We also conducted manual measurements of the depth and diameter of CHs two to four times during the 2014 and 2017
summer seasons. In addition, we used the dates of the CH collapse events reported by Takeuchi et al. (2018) for model
evaluation. CH depths and diameters were manually measured from 20 to 50 randomly selected CHs at each site. Averages
230   and standard deviations of the observed depths and diameters are summarised in Table 2.

4. Experimental design of the model evaluation and sensitivity tests

     To evaluate CryHo, numerical simulations of the CH depth were conducted at several sites of the Qaanaaq ice cap for the
three summer seasons (Site-exp). The number of study sites in 2012, 2014, and 2017 were one (Site 3), four (Sites 1 to 4), and
three (Sites 1 to 3), respectively. The depths and diameters observed on the first observational date were used to set the model
235   constants at each site (D_0 and ϕ in Table 2). The meteorological data measured at Site 5 were used as input for the simulations.
At each site, T_a was corrected based on the air temperature measured at Site 5 and a temperature lapse rate of -7.80×10^{-3} °C
m^{-1}, which had been previously estimated from field observations on the same glacier in 2012 (Sugiyama et al., 2014). The
other meteorological data at each site were assumed to be the same as those measured at Site 5. The observed surface
temperature at Site 5 was almost 0 °C during the three observational periods; thus, it was safely used also as input for the other
240   sites, since they were located at lower elevations than that of Site 5 (Fig. 3). In 2014, α_i at Sites 1, 2, 3, and 4 was assumed to
be 0.68, 0.57, 0.40, and 0.41, respectively (Table 2), as mentioned in Sect. 3.2. Similarly, in 2017, α_i at Sites 1, 2, and 3 was
assumed to be 0.56, 0.42, and 0.24, respectively (Table 2). α_i in 2012 for Site 3 was assumed to be 0.4, as observed by Takeuchi

et al. (2018). We assumed the albedo at the CH bottom (α_c) to be 0.1 based on assumptions and observations in previous studies (e.g., Takeuchi et al., 2001; Jepsen et al., 2010). The calculation periods for the simulations in 2014 and 2017 were taken from the first date when CH depths were measured in June or July. In the 2012 simulation, the period was constrained by both CH and AWS observations.

We conducted sensitivity tests to assess the sensitivity of the CH depth to input data and model constants, such as air temperature (T_a-exp), radiation components (R_S-exp), initial depth (D_0-exp), hole diameter (ϕ-exp), albedo at the ice surface (α_i-exp), albedo at the CH bottom (α_c-exp), and extinction coefficients of direct (κ_d-exp) and diffuse (κ_f-exp) radiation (Table 3). Site-exp, i.e., Site 2 in 2014, was used as the control experiment for the sensitivity tests (Ctl-exp). The ranges of the changing parameters, which are summarised in Table 3, were determined based on field measurements (Table 2). The extinction coefficients for κ_d-exp and κ_f-exp were obtained from multiplying by factors of 0.25–4.00 the original values. The factor range was assumed by referring to the difference between the spectral flux extinction coefficient and absorption coefficient calculated from the imaginary refractive index of pure ice (Fig. S4). In R_S-exp, we assumed r_{dif} of Eqs (9) and (10) to be 0 and 1 in Sd and Sf cases shown in Table 3, respectively. Note that the extinction coefficients of ice (i.e., κ_d and κ_f) are same as each other in R_S-exp.

To quantify the four components of shortwave radiation reaching the CH bottom (R_{Sdc}, R_{Sfc}, R_{Stdc}, and R_{Stfc}) for different CH geometries (i.e., depths and diameters), we conducted two sensitivity tests ($R_{Sc}D$-exp and $R_{Sc}\phi$-exp, respectively) at 14:00 local time on DOY 172 (i.e., the time of meridian transit at the summer solstice) in 2014. The CH depth and diameter ranged from 10 to 350 mm in $R_{Sc}D$-exp and from 10 to 150 mm in $R_{Sc}\phi$-exp, respectively. The CH diameter and depth were assumed to be 50 mm in $R_{Sc}D$-exp and 10 mm in $R_{Sc}\phi$-exp, respectively. The other model constants were the same as those in Ctl-exp.

To discuss the meteorological factors controlling the CH dynamics, besides the sensitivity tests described above, we also investigated the relationships between the CH deepening or shallowing rates against the input meteorological conditions, and the simulated heat properties at the ice surface at the CH bottom. These relationships were obtained from the input and output data in Ctl-exp. The deepening (shallowing) rate (mm h^{-1}) was calculated when a CH deepened (shallowed) compared to its state one hour earlier.

5. Results and discussion

5.1. Evaluation of the cryoconite hole depth

The CH depth simulations at the different elevation sites in the three years (Site-exp) showed that the simulated temporal changes in CH depth, including CH collapse, agreed well with those observed at all sites for the three years (Figs 5 and 6). The CH depth observed by both the camera and manual measurements at Site 2 gradually shallowed from DOY 186 to 202, developed until DOY 212, and shallowed again until DOY 215 (Fig. 5b). The modelled and camera-based CH depths at this site were in good agreement with each other ($R^2 = 0.81$; root mean square error of 30.5 mm). In addition, the model also

simulated the CH collapse event between DOY 202 and 204, during which the camera-based CH depth was not recorded (line
275   gap in Fig. 5b). The model simulations revealed the good performance of the model also at the other sites (Figs 5a, 5c, and
5d). Although no CH depth measurement was conducted in 2012, the model captured the CH collapses observed at Site 3 on
DOY 206 and 208 (Fig. 6a, grey dashed lines). The manual measurements in 2017 showed similar temporal changes in CH
depth to those in 2014 (Figs 6b–d), which were also well represented by the model, especially the timing of drastic CH decays
around DOY 210 at all sites. Because CryHo diagnoses the CH depth based on the balance between melt at the ice surface
280   (M_i) and at the CH bottom (M_c), the model can capture the CH decay dynamics, which have not been simulated by previous
numerical models considering only M_c (Gribbon, 1979; Jepsen et al., 2010; Cook, 2012). This indicates that the concept of
CryHo, in which both heat balances (i.e., M_i and M_c) control the temporal change in the development and decay of CHs, is
essentially correct. In the next section, we discuss in detail the meteorological and/or ice physical factors that are important
for simulating temporal changes.

285   **5.2. Sensitivity of the simulated hole depth to the model parameters**

The sensitivity experiment regarding the air temperature (T_a-exp) suggests that CHs tend to be deeper and more stable under
cooler conditions, and vice versa (Fig. 7a). This is likely because the turbulent heat fluxes on the ice surface decrease under
cooler conditions; thus, net radiation becomes the main component for ice melting, which is constrained by the albedo at the
ice surface and CH bottom. Indeed, field observations indicated that the turbulent heat fluxes during warmer conditions (DOY
290   198–205) were increased compared to the case during cooler conditions (before DOY 198) at Site 2 in 2014 (Fig. S5). Under
such cooler conditions, the melt rate at the ice surface surrounding the CHs was lower, resulting in deeper and therefore more
stable CHs. Indeed, Gribbon (1979) reported that the CH depth increased with the elevation of the glacier in West Greenland.
Furthermore, higher melt rates (hence, warmer conditions) at the ice surface are likely to induce CH decay, as suggested by
Hodson et al. (2007). Therefore, global warming may cause the collapse of CHs earlier in the melt season compared to the
295   present case, thereby inducing darkening of the ice surface by cryoconite granule redistribution in the future. Nevertheless, a
snow–ice–atmosphere coupling simulation using a climate model coupled with CryHo is necessary to evaluate the contribution
of CH dynamics to surface darkening under climate change.

The sensitivity experiment regarding the shortwave radiation components (R_S-exp) suggests that the dominant direct and
diffuse components contribute to the decay and development of CHs, respectively (Fig. 7b), which suggests that the diffuse
300   component significantly contributes to CH development rather than the direct component. We then compared the contributions
of each radiation component reaching the CH bottom during the experiment period (Fig. S6, blue and red lines). The CH
bottom is more accessible by the diffuse component ($R_{Sfc} + R_{Stfc}$) rather than the direct component ($R_{Sdc} + R_{Stdc}$), except
for shallowing depth case. In the model, the direct component of shortwave radiation can reach the CH bottom only when the
solar zenith angle θ_z is smaller than the CH edge θ_c (Fig. 1 and Eq. 15) and it is transmitted through the ice in the opposite
305   case. Because θ_z and θ_c ranged from 56 to 85° and 8 to 90° during the simulation period at the studied glacier, respectively,

the direct component reaching the CH bottom from the hole mouth was very limited. Indeed, the total diffuse component reaching the CH bottom was larger than the total direct component even at the summer solstice, except for the CH depth of 10 mm case (Fig. 8a). To investigate heat flux to the CH bottom by shortwave radiation from the hole mouth or through the ice, we additionally compared the contributions of each radiation component reaching the CH bottom (Fig. S6, grey lines). The

310   figure depicts that the radiation components transmitted through ice to the CH bottom ($R_{Stfc} + R_{Stdc}$) was greater than the radiation components reaching the CH bottom from the hole mouth ($R_{Sfc} + R_{Sdc}$) when CH developed from DOY 208 to 213, meaning that radiation components transmitted through ice are also important for the heat balance at the CH bottom (i.e., Q_c). Further discussion regarding shortwave radiation transmitted throughout the ice is described later.

The sensitivity experiments regarding the CH geometry (D_0-exp and ϕ-exp) suggest that differences in the geometrical

315   parameters have little influence on the CH depth. The simulated CH depth starting from different initial depths converged within approximately two weeks (Fig. 7c). This is probably because the CH bottom is relatively accessible by shortwave radiation in the case of shallower depths, and vice versa (Fig. 8a), which is quantified by additional experiments ($R_{Sc}D$-exp and $R_{Sc}\phi$-exp). The diameter shows no significant effect on the CH depth (Fig. 7d), although it strongly affects whether shortwave radiation reaches the CH bottom. This is likely because transmitted shortwave radiation reaches the CH bottom

320   irrespective of the CH diameter. Figure 8b suggests no significant difference in the total shortwave radiation reaching the CH bottom among the different diameters, thereby supporting the ϕ-exp result. Indeed, no significant correlation between the CH depth and diameter has been found (Gribbon, 1979). Furthermore, the observed CH depths and diameters significantly varied among the sites and years (Tables 2 and S2), suggesting that CH depth is mainly controlled by factors other than the CH diameter.

325   The sensitivity experiments regarding the albedos of the ice surface and CH bottom (α_i-exp and α_c-exp) suggest that the boundary condition of the ice surface (α_i) is a more important parameter than that of the CH bottom (α_c) for reproducing the CH dynamics, especially the timing of CH collapse. The CH depth increases with an increase in α_i owing to decreasing M_i, whereas it decreases with an increase in α_c owing to decreasing M_c (Figs 7e, 7f). Notably, the sensitivity of the CH depth to α_i was greater than that to α_c. This is probably because shortwave radiation at the ice surface was greater than that at the CH

330   bottom. In addition, α_i-exp suggests that a 0.1 decrease in α_i induces CH collapse one day earlier. Although α_c is known to be a key parameter for simulating the CH deepening rate (Podgorny and Grenfell, 1996), there is little information and discussions regarding α_i. Our results highlight for the first time the importance of both α_i and α_c in simulating vertical CH variations. Furthermore, the collapse of CHs is likely to reduce the ice surface albedo, owing to the redistribution of cryoconite on the ice surface (Irvine-Fynn et al., 2011; Takeuchi et al., 2018). Considering studies that reported a darkening trend of the

335   GrIS surface over the last 20 years (e.g., Shimada et al., 2016; Tedstone et al., 2017), a positive albedo feedback, during which a decrease in ice surface albedo causes frequent CH collapse events, may occur. While our assumed reflectance was based on the α_i observations in 2014, the ice surface albedo should change temporally. The uncertainty of the model simulations, such as that regarding the results around DOY 204 at Site 3 in 2017 (Fig. 6d), may be attributed to temporal changes in the ice

surface albedo. To simulate the development and decay of CHs more accurately, temporal changes in the ice surface albedo,
340   including the effects of CH collapse and algal blooms, should be incorporated into CryHo.

The sensitivity experiments regarding the broadband extinction coefficients of shortwave radiation transmitted throughout
ice for the direct and diffuse components (κ_d-exp and κ_f-exp) suggest that κ_d is more effective at the CH depth than κ_f. Both
experiments showed that the CH depth with a higher coefficient was shallower, owing to a decrease in M_c (Figs 7g and 7h);
however, there was a significant difference in the sensitivity to the coefficients, even though both parameters were the same,
345   as in Eq. (25). As discussed for the R_S-exp, the direct component of shortwave radiation is transmitted throughout the ice rather
than the diffuse component. Indeed, Figure 8 indicates that all of the direct component of shortwave radiation is transmitted
throughout the ice in the case of $\theta_z > \theta_c$ (R_{Stdc}), whereas the CH bottom is directly accessible by a part of the diffuse
component (R_{Sfc}). This is probably the cause of the higher sensitivity to κ_d, suggesting that κ_d is likely a relatively more
important parameter compared to κ_f. However, there was no significant difference in sensitivity between κ_f and κ_d in the case
350   of $\theta_z \leq \theta_c$, which is the case for depths shallower than approximately 50 mm in Figs 7g and 7h. In such a case, most of the
direct and diffuse components reach the CH bottom without being transmitted through the ice (Fig. 8). Figure 8 also suggests
that shortwave radiation transmitted throughout the ice is dominant in the opposite case. Since CH depth ranged from 0 to 200
mm at Site 2 in 2014, the result supports our argument that transmitted shortwave radiation mainly contribute to CH
development as described in the paragraph of Rs-exp. In Antarctic, a lot of CHs of over 300 mm depth were reported even
355   though the CH mouths were covered with frozen ice (Fountain et al., 2004), suggesting that the contribution of the transmitted
shortwave radiation to CH development. The results highlight the importance of separating the direct and diffuse components
of shortwave radiation in CH depth simulations. Further studies on the optical characteristics of ice are necessary, because
there is little information on the broadband flux extinction coefficients.

5.3. Meteorological factors controlling the cryoconite hole dynamics

360   Downward shortwave radiation governs the CH deepening processes (Hodson et al., 2010a; Takeuchi et al., 2018). To better
understand the factors controlling the CH deepening and shallowing processes, we compared the heat components with both
the CH deepening and shallowing rates. In the shallowing phase (red marks in Fig. 9), CH decay is mainly controlled by the
sensible and latent heat fluxes at the ice surface (H_{Si} and H_{Li}) via wind speed (U). Air temperature (T_a) shows no significant
correlation with the shallowing rate; conversely, U shows a strong correlation with the shallowing rate (Figs 9a and 9d).
365   However, there is no clear relationship between the input downward shortwave radiation, input downward longwave radiation,
relative humidity, and direct and diffuse components of downward shortwave radiation at the ice surface (R_S, R_L, h_r, R_{Sd} and
R_{Sf} shown in Figs 9b, 9c, 9e, 9 g, and 9h, respectively). The results suggest that strong winds induce CH decay by increasing
the surface melt via the turbulent heat fluxes (Figs 9f, 9i, and 9j). Takeuchi et al. (2018) suggested that CHs tend to be shallower
under both cloudy and windy conditions. Our analyses also suggest that windy conditions are important meteorological
370   conditions governing the CH decay. However, cloudy conditions may contribute to the CH development because the diffuse

component of downward shortwave radiation generally increases under cloudy conditions. According to Figure 10a, CHs tend to be shallower when the wind is strong (i.e., above 8 m s^{-1}) and the diffuse component of downward shortwave radiation is weak (i.e., below 200 W m^{-2}). During the period when two CH collapse events were observed at the Qaanaaq ice cap by Takeuchi et al. (2018), meteorological conditions met the requirements for CH decay, as suggested by our simulation. This is probably the reason why the CH collapse events were observed under cloudy conditions.

In the CH deepening phase (blue marks in Fig. 9), although the input shortwave radiation (R_S) was weakly correlated with the CH deepening rate, the diffuse component reaching the CH bottom was strongly correlated with the CH deepening rate ($R_{Sfc} + R_{Stfc}$), whereas no correlation was found with the direct component reaching the CH bottom ($R_{Sdc} + R_{Stdc}$) (Figs 9l and 9m). Furthermore, Fig. 9k, which shows the relationship between ice melt at the CH bottom (Q_c) and the CH deepening rate, is similar to Fig. 9m. The results suggest an essential contribution of the diffuse component to CH development, which was also revealed by sensitivity analysis. However, the direct component strongly depends on the solar zenith angle and CH geometry (θ_z and θ_c); thus, the CH development is likely to be unstable during sunny conditions. Other meteorological variables are unlikely to contribute to the CH development. Although previous studies suggested that sunny conditions induce CH development (Hodson et al., 2010b; Irvine-Fynn et al., 2011; Takeuchi et al., 2018), our results highlight that the diffuse component of shortwave radiation is a key factor governing CH development, rather than merely sunny conditions. Because the CH deepening rate is likely to depend on wind speed and the intensity of the diffuse component of downward shortwave radiation, as shown in Figure 10b, CHs could develop under sunny conditions depending on wind speed and other meteorological conditions. CH depths are mainly determined by the balance between the intensity of the diffuse component of downward shortwave radiation and the strength of the wind speed.

5.4. Other possible factors affecting cryoconite hole dynamics

Our model does not include the effect of water lingering in CHs on the heat balance at the CH bottom because a quantitative understanding of the mechanism of convective heat transport or the buffering effect in the lingering water is insufficient. Such lingering water in CHs may affect the heat exchange between the atmosphere and CH bottom. Heat exchange should not be negligible in the case of large water surfaces in CHs. Besides lingering water in CHs, the thickness of cryoconite at the CH bottom, which is not considered by CryHo, is also likely to be a key factor in determining the CH diameter and shape (Cook et al., 2010). Furthermore, the surface slope of the glacier affects the sediment thickness and, thus, the CH shape geometry via water flow and changes the shortwave radiation reaching the CHs (Takeuchi et al., 2000; Cook et al., 2018). Although such factors should be incorporated into CryHo in the future, CryHo is likely to reproduce well the temporal change in CH depth, in the case of a cylindrical CH on a rather flat surface with a diameter of 100 mm, which falls within the range of CH shape geometries documented in this study. Compared to the effects of CH shape geometry and topological conditions, the effects of lingering water and sediment thickness in CHs on the CH depth may be small. The CH diameter range is similar to that observed in glaciers in West Greenland, Svalbard, and the Himalayas (Gribbon, 1979; Takeuchi et al., 2000; Cook et al., 2010), suggesting that CryHo can be applied also to these regions.

6. Conclusions

405   We established a numerical cryoconite hole model (CryHo) to reproduce the vertical cryoconite hole (CH) dynamics. We evaluated the model using field observations from an ice cap in Northwest Greenland, collected during the 2012, 2014, and 2017 summer seasons. The CryHo simulates the temporal changes in CH depth based on heat balances calculated independently at the ice surface and the CH bottom. This is a novel concept that is different from previous models simulating the CH development. CryHo considers also the CH geometry, which affects the direct and diffuse components of shortwave
410   radiation, while including the optical process of transmitted radiation throughout ice. Field observations revealed that CHs repeatedly developed and decayed over time. CryHo reasonably reproduced the observed temporal changes in CH depth, including the CH shallowing phase at four sites during three melt seasons. Sensitivity tests indicated that the CH bottom is relatively accessible by the diffuse component— rather than the direct component—of shortwave radiation, thereby controlling the CH development. In addition, both component of shortwave radiation transmitted throughout ice also significantly
415   contribute to CH development, except for shallowing CH or large diameter cases. Besides wind speed, which has been indicated by earlier studies, we revealed that ice surface albedo is also an important factor affecting the timing of the CH collapse. Although many studies in Greenland have reported the bio-albedo effect contributing to ice surface darkening, CH collapse could also reduce the ice surface albedo not only by redistributing the cryoconite granules, but also by increasing the phototrophic (i.e., algae, cyanobacteria, diatoms, etc.) and heterotrophic (i.e., tardigrade, rotifer, etc.) communities. Therefore,
420   CHs dynamics are interactively connected to physical and microbiological processes on the ice surface. For improved projection of spatiotemporal changes in the bio-albedo effect, CryHo will be useful when coupled with regional or global climate models, although additional observations and model evaluation in various glaciers and ice sheets are necessary.

Code and Data availability

The codes of the model as well as the analysis and observational data used in this study are available at the following reference:
425   https://doi.org/10.5281/zenodo.7539526 (Onuma et al., 2023). Meteorological observations from the SIGMA-B site are available at https://ads.nipr.ac.jp/data/meta/A20220413-006/ (Nishimura et al., 2021).

Author contributions

KF designed the study. YO, NT, and TA designed the study. KF developed the model with the support of MN and TA. TA parameterized the extinction coefficients of ice. All authors performed field observations. YO and KF analysed the data and
430   wrote the manuscript. All authors contributed to the discussion.

Competing interests. Masashi Niwano is a member of the editorial board of the journal The Cryosphere.

Acknowledgements

This work was supported by the Arctic Challenge for Sustainability (ArCS, JPMXD130000000), Arctic Challenge for
435 Sustainability II (ArCS II, JPMXD1420318865), and Advanced Studies of Climate Change Projection (SENTAN, JPMXD0722680395) from the Ministry of Education, Culture, Sports, Science and Technology (MEXT), Japan. This study was also partly supported by Grant-in-Aids (JP23221004, JP26247078, JP26241020, JP16H01772, 16H06291, JP19H01143, JP20K19955, and JP21H03582). We thank J. Uetake, N. Nagatsuka, R. Shimada, S. Tanaka, R. Sakaki, K. Ishiwatari, and A. Watanabe for their support with the field observations.

440 **References**

Aoki, T., Aoki, T., Fukabori, M., Hachikubo, A., Tachibana, Y., and Nishio, F.: Effects of snow physical parameters on spectral albedo and bidirectional reflectance of snow surface, J. Geophys. Res., 105, 10219–10236. https://doi.org/10.1029/1999JD901122, 2000.

Aoki, T., Aoki, T., Fukabori, M., and Uchiyama, A.: Numerical simulation of the atmospheric effects on snow albedo with a
445   multiple scattering radiative transfer model for the atmosphere-snow system, J. Meteorol. Soc. Jpn, 77, 595–614. https://doi.org/10.2151/jmsj1965.77.2_595, 1999.

Aoki, T., Matoba, S., Uetake, J., Takeuchi, N., and Motoyama, H.: Field activities of the "Snow Impurity and Glacial Microbe effects on abrupt warming in the Arctic" (SIGMA) project in Greenland in 2011–2013, Bull. Glaciol. Res., 32, 3–20. https://doi.org/10.5331/bgr.32.3, 2014.

450 Bøggild, C. E., Brandt, R. E., Brown, K. J., and Warren, S. G.: The ablation zone in northeast Greenland: Ice types, albedos and impurities, J. Glaciol., 56, 101–113. https://doi.org/10.3189/002214310791190776, 2010.

Chandler, D. M., Alcock, J. D., Wadham, J. L., Mackie, S. L., and Telling, J.: Seasonal changes of ice surface characteristics and productivity in the ablation zone of the Greenland Ice Sheet, The Cryosphere, 9, 487–504. https://doi.org/10.5194/tc-9-487-2015, 2015.

455 Cook, J.: Microbially mediated carbon fluxes on the surface of glaciers and ice sheets. PhD Thesis, University of Sheffield, UK, 2012.

Cook, J. M., Hodson, A. J., and Irvine-Fynn, T. D. L.: Supraglacial weathering crust dynamics inferred from cryoconite hole hydrology, Hydrol. Processes., 30, 433–446. https://doi.org/10.1002/hyp.10602, 2016.

Cook, J. M., Sweet, M., Cavalli, O., Taggart, A., and Edwards, A.: Topographic shading influences cryoconite
460   morphodynamics and carbon exchange, Arct. Antarct. Alp. Res., 50, S100014. https://doi.org/10.1080/15230430.2017.1414463, 2018.

Cook, J., Edwards, A., Takeuchi, N., and Irvine-Fynn, T.: Cryoconite: The dark biological secret of the cryosphere, Prog. Phys. Geogr., 40, 66–111. https://doi.org/10.1177/0309133315616574, 2016.

Cook, J., Hodson, A., Telling, J., Anesio, A., Irvine-Fynn, T., and Bellas, C.: The mass–area relationship within cryoconite
465   holes and its implications for primary production, Ann. Glaciol., 51, 106–110. https://doi.org/10.3189/172756411795932038, 2010.

Cooper, M. G., Smith, L. C., Rennermalm, A. K., Tedesco, M., Muthyala, R., Leidman, S. Z., Moustafa, S. E., and Fayne, J. V.: Spectral attenuation coefficients from measurements of light transmission in bare ice on the Greenland Ice Sheet, Cryosphere, 15, 1931–1953. https://doi.org/10.5194/tc-15-1931-2021, 2021.

470 Fountain, A. G., Tranter, M., Nylen, T. H., Lewis K. J., and Mueller, D. R.: Evolution of cryoconite holes and their contribution to meltwater runoff from glaciers in the McMurdo Dry Valleys, Antarctica, J. Glaciol., 50, 35–45. https://doi.org/10.3189/172756504781830312, 2004.

Fountain, A. G., Nylen, T. H., Tranter, M., and Bagshaw, E.: Temporal variations in physical and chemical features of cryoconite holes on Canada Glacier, McMurdo Dry Valleys, Antarctica, J. Geophys. Res. Biogeosci., 113, G01S92. https://doi.org/10.1029/2007JG000430, 2008.

Goudriaan, J.: Crop micrometeorology: A simulation study, Pudoc, Wageningen, and Netherlands, 1977.

Gribbon, P. W. F.: Cryoconite holes on Sermikavsak, West Greenland, J. Glaciol., 22, 177–181. https://doi.org/10.3189/S0022143000014167, 1979.

Hodson, A., Anesio, A. M., Ng, F., Watson, R., Quirk, J., Irvine-Fynn, T., Dye, A., Clark, C., McCloy, P., Kohler, J., Sattler, B.: A glacier respires: Quantifying the distribution and respiration CO_2 flux of cryoconite across an entire Arctic supraglacial ecosystem, J. Geophys. Res., 112, G04S36. https://doi.org/10.1029/2007JG000452, 2007.

Hodson, A., Anesio, A. M., Tranter, M., Fountain, A., Osborn, M., Priscu, J., Laybourn-Parry, J., Sattler, B.: Glacial ecosystems, Ecol. Monogr., 78, 41–67. https://doi.org/10.1890/07-0187.1, 2008.

Hodson, A., Bøggild, C., Hanna, E., Huybrechts, P., Langford, H., Cameron, K., and Houldsworth, A.: The cryoconite ecosystem on the Greenland ice sheet, Ann. Glaciol., 51, 123–129. https://doi.org/10.3189/172756411795931985, 2010a.

Hodson, A., Cameron, K., Bøggild, C., Irvine-Fynn, T., Langford, H., Pearce, D., and Banwart, S.: The structure, biological activity and biogeochemistry of cryoconite aggregates upon an arctic valley glacier: Longyearbreen, Svalbard, J. Glaciol., 56, 349–362. https://doi.org/10.3189/002214310791968403, 2010b.

Holland, A. T., Williamson, C. J., Sgouridis, F., Tedstone, A. J., McCutcheon, J., Cook, J. M., Poniecka, E., Yallop, M. L., Tranter, M., Anesio, A. M., and the Black & Bloom Group: Dissolved organic nutrients dominate melting surface ice of the Dark Zone (Greenland Ice Sheet), Biogeosciences, 16, 3283–3296. https://doi.org/10.5194/bg-16-3283-2019, 2019.

Irvine-Fynn, T. D. L., Bridge, J. W., and Hodson, A. J.: In situ quantification of supraglacial cryoconite morphodynamics using time-lapse imaging: An example from Svalbard, J. Glaciol., 57, 651–657. https://doi.org/10.3189/002214311797409695, 2011.

Irvine-Fynn, T. D. and Edwards, A.: A frozen asset: The potential of flow cytometry in constraining the glacial biome, Cytometry A, 85, 3–7. https://doi.org/10.1002/cyto.a.22411, 2014.

Jepsen, S. M., Adams, E. E., and Priscu, J. C.: Sediment melt-migration dynamics in perennial Antarctic lake ice, Arct. Antarct. Alp. Res., 42, 57–66. https://doi.org/10.1657/1938-4246-42.1.57, 2010.

Langford, H., Hodson, A., Banwart, S., and Bøggild, C.: The microstructure and biogeochemistry of arctic cryoconite granules, Ann. Glaciol., 51, 87–94. https://doi.org/10.3189/172756411795932083, 2010.

McIntyre, N. F.: Cryoconite hole thermodynamics, Can. J. Earth Sci., 21, 152–156. https://doi.org/10.1139/e84-016, 1984.

Nishimura, M., Aoki, T., Niwano, M., Matoba, S., Tanikawa, T., Yamaguchi, S., Yamasaki, T., and Fujita, K.: Quality-controlled datasets of automatic weather station (AWS) at sigma-B site from 2012 to 2020: Level 1.3. https://ads.nipr.ac.jp/data/meta/A20220413-006/, Arctic Data Archive System (ADS), Japan, 2021.

Onuma, Y., Fujita, K., Takeuchi, N., Niwano, M., and Aoki, T.: Codes and data set for Cryoconite hole model (CryHo): Version 0. https://doi.org/10.5281/zenodo.7539526, Zenodo, 2023.

Podgorny, I. A. and Grenfell, T. C.: Absorption of solar energy in a cryoconite hole, Geophys. Res. Lett., 23, 2465–2468. https://doi.org/10.1029/96GL02229, 1996.

Schneider, C. A., Rasband, W. S., and Eliceiri, K. W.: NIH Image to ImageJ: 25 years of image analysis, Nat. Methods, 9, 671–675. https://doi.org/10.1038/nmeth.2089, 2012.

Shimada, R., Takeuchi, N., and Aoki, T.: Inter-annual and geographical variations in the extent of bare ice and dark ice on the Greenland ice sheet derived from MODIS satellite images, Front. Earth Sci., 4, 43. https://doi.org/10.3389/feart.2016.00043, 2016.

Stibal, M., Box, J. E., Cameron, K. A., Langen, P. L., Yallop, M. L., Mottram, R. H., Khan, A. L., Molotch, N. P., Chrismas, N. A. M., Quaglia, F. C., Remias, D., Smeets, C. J. P. P., van den Broeke, M. R., Ryan, J. C., Hubbard, A., Tranter, M., van As, D., and Ahlstrøm, A. P.: Algae drive enhanced darkening of bare ice on the Greenland ice sheet, Geophys. Res. Lett., 44, 11463–11471. https://doi.org/10.1002/2017GL075958, 2017.

Stibal, M., Tranter, M., Benning, L. G., and Řehák, J.: Microbial primary production on an Arctic glacier is insignificant in comparison with allochthonous organic carbon input, Environ. Microbiol., 10, 2172–2178. https://doi.org/10.1111/j.1462-2920.2008.01620.x, 2008.

Sugiyama, S., Sakakibara, D., Matsuno, S., Yamaguchi, S., Matoba, S., and Aoki, T.: Initial field observations on Qaanaaq ice cap, northwestern Greenland, Ann. Glaciol., 55, 25–33. https://doi.org/10.3189/2014AoG66A102, 2014.

Takeuchi, N., Fujisawa, Y., Kadota, T., Tanaka, S., Miyairi, M., Shirakawa, T., Kusaka, R., Fedorov, A. N., Konstantinov, P., and Ohata, T.: The effect of impurities on the surface melt of a glacier in the Suntar-Khayata mountain range, Russian Siberia, Front. Earth Sci., 3, 82. https://doi.org/10.3389/feart.2015.00082, 2015.

Takeuchi, N., Kohshima, S., and Seko, K.: Structure, formation, and darkening process of albedo-reducing material (cryoconite) on a Himalayan glacier: A granular algal mat growing on the glacier, Arct. Antarct. Alp. Res., 33, 115–122. https://doi.org/10.1080/15230430.2001.12003413, 2001.

Takeuchi, N., Kohshima, S., Yoshimura, Y., Seko, K., and Fujita, K.: Characteristics of cryoconite holes on a Himalayan glacier, Yala Glacier Central Nepal, Bull. Glaciol. Res., 17, 51–59, 2000.

Takeuchi, N., Nagatsuka, N., Uetake, J., and Shimada, R.: Spatial variations in impurities (cryoconite) on glaciers in northwest Greenland, Bull. Glaciol. Res., 32, 85–94. https://doi.org/10.5331/bgr.32.85, 2014.

Takeuchi, N., Nishiyama, H., and Li, Z.: Structure and formation process of cryoconite granules on Ürümqi glacier No. 1, Tien shan, China, Ann. Glaciol., 51, 9–14. https://doi.org/10.3189/172756411795932010, 2010.

Takeuchi, N., Sakaki, R., Uetake, J., Nagatsuka, N., Shimada, R., Niwano, M., and Aoki, T.: Temporal variations of cryoconite holes and cryoconite coverage on the ablation ice surface of Qaanaaq Glacier in northwest Greenland, Ann. Glaciol., 59, 21–30. https://doi.org/10.1017/aog.2018.19, 2018.

Tedstone, A. J., Bamber, J. L., Cook, J. M., Williamson, C. J., Fettweis, X., Hodson, A. J., and Tranter, M.: Dark ice dynamics of the south-west Greenland Ice Sheet, The Cryosphere, 11, 2491–2506. https://doi.org/10.5194/tc-11-2491-2017, 2017.

540   Tedstone, A. J., Cook, J. M., Williamson, C. J., Hofer, S., McCutcheon, J., Irvine-Fynn, T., Gribbin, T., and Tranter, M.: Algal growth and weathering crust state drive variability in western Greenland Ice Sheet ice albedo, The Cryosphere, 14, 521–538. https://doi.org/10.5194/tc-14-521-2020, 2020.

Tsutaki, S., Sugiyama, S., Sakakibara, D., Aoki, T., and Niwano, M.: Surface mass balance, ice velocity and near-surface ice temperature on Qaanaaq Ice Cap, northwestern Greenland, from 2012 to 2016, Ann. Glaciol., 58, 181–192.
545   https://doi.org/10.1017/aog.2017.7, 2017.

Uetake, J., Nagatsuka, N., Onuma, Y., Takeuchi, N., Motoyama, H., and Aoki, T.: Bacterial community changes with granule size in cryoconite and their susceptibility to exogenous nutrients on NW Greenland glaciers, FEMS Microbiol. Ecol., 95, fiz075. https://doi.org/10.1093/femsec/fiz075, 2019.

Uetake, J., Tanaka, S., Segawa, T., Takeuchi, N., Nagatsuka, N., Motoyama, H., and Aoki, T.: Microbial community variation
550   in cryoconite granules on Qaanaaq Glacier, NW Greenland, FEMS Microbiol. Ecol., 92, fiw127. https://doi.org/10.1093/femsec/fiw127, 2016.

Wang, S., Tedesco, M., Alexander, P., Xu, M., and Fettweis, X.: Quantifying spatiotemporal variability of glacier algal blooms and the impact on surface albedo in southwestern Greenland, Cryosphere, 14, 2687–2713. https://doi.org/10.5194/tc-14-2687-2020, 2020.

555   Wharton, R. A., McKay, C. P., Simmons, G. M., and Parker, B. C.: Cryoconite holes on glaciers, BioScience, 35, 499–503. https://doi.org/10.2307/1309818, 1985.

Wientjes, I. G. M., Van de Wal, R. S. W., Reichart, G. J., Sluijs, A., and Oerlemans, J.: Dust from the dark region in the western ablation zone of the Greenland ice sheet, Cryosphere, 5, 589–601. https://doi.org/10.5194/tc-5-589-2011, 2011.

Williamson, C. J., Cook, J., Tedstone, A., Yallop, M., McCutcheon, J., Poniecka, E., Campbell, D., Irvine-Fynn, T., McQuaid,
560   J., Tranter, M., Perkins, R., and Anesio, A.: Algal photophysiology drives darkening and melt of the Greenland Ice Sheet, Proc. Natl Acad. Sci. U. S. A., 117, 5694–5705. https://doi.org/10.1073/pnas.1918412117, 2020.

Zawierucha, K., Porazinska, D. L., Ficetola, G. F., Ambrosini, R., Baccolo, G., Buda, J., Ceballos, J. L., Devetter, M., Dial, R., Franzetti, A., Fuglewicz, U., Gielly, L., Łokas, E., Janko, K., Novotna Jaromerska, T., Kościński, A., Kozłowska, A., Ono, M., Parnikoza, I., Pittino, F., Poniecka, E., Sommers, P., Schmidt, S.K., Shain, D., Sikorska, S., Uetake, J., and
565   Takeuchi, N.: A hole in the nematosphere: tardigrades and rotifers dominate the cryoconite hole environment, whereas nematodes are missing, J. Zool., 313, 18–36, https://doi.org/10.1111/jzo.12832, 2021.

Table 1: Variables and constants used in the Cryoconite hole model (CryHo). Variables having different surfaces are indicated by an asterisk in the subscript, i indicates ice surface and c indicates cryoconite hole (CH) bottom. [+] denotes the input data.

Symbol	Variable or constant	Unit and value
T_a	Air temperature[+]	°C
h_r	Relative humidity[+]	-
P_a	Air pressure[+]	hPa
U	Wind speed[+]	m s^{-1}
R_S	Downward shortwave radiation[+]	W m^{-2}
R_L	Downward longwave radiation[+]	W m^{-2}
R_{Lui}	Upward longwave radiation[+]	W m^{-2}
α_i	Surface albedo at ice surface	0.24 – 0.68 (see Table 2)
α_c	Surface albedo at CH bottom	0.1
ε	Emissivity of the ice surface	1.0
σ	Stefan–Boltzmann constant	5.67×10^{-8} W m^{-2} K^{-4}
c_p	Specific heat of air	1006 J K^{-1} kg^{-1}
C	Bulk coefficient for snow-ice surface	0.0025
l_E	Latent heat for water evaporation	2.50×10^6 J kg^{-1}
l_M	Latent heat for ice melting	3.33×10^5 J kg^{-1}

t_h	Length of an hour in seconds	3600 s
ρ_i	Ice density	900 kg m^{-3}
ρ_w	Water density	1000 kg m^{-3}
D_0	Initial depth	mm
ϕ	Hole diameter	mm
M_*	Hourly amount of ice melt	mm w. e. h^{-1}
Q_{M*}	Excess heat energy for ice melting	W m^{-2}
Q_*	Heat balance	W m^{-2}
T_i	Ice surface temperature	°C
H_{S*}	Sensible heat flux	W m^{-2}
H_{L*}	Latent heat flux	W m^{-2}
R_{Ln*}	Net longwave radiation	W m^{-2}
R_{Lc}	Longwave radiation from the sky looking up from the CH bottom	W m^{-2}
R_{Lw}	Longwave radiation from the CH wall	W m^{-2}
R_{Sd}	Direct component of shortwave radiation	W m^{-2}
R_{Sf}	Diffuse component of shortwave radiation	W m^{-2}
R_{Sdc}	Direct component of shortwave radiation reaching the CH bottom	W m^{-2}
R_{Sfc}	Diffuse component of shortwave radiation reaching the CH bottom	W m^{-2}

R_{Stdc}	Direct component of shortwave radiation transmitted through ice to the CH bottom	W m^{-2}
R_{Stfc}	Diffuse component of shortwave radiation transmitted through ice to the CH bottom	W m^{-2}
ρ_a	Air density	kg m^{-3}
$q(T)$	Saturated specific humidity	kg kg^{-1}
r_{dif}	Diffuse ratio of downward shortwave radiation	-
r_{ze}	Ratio based on solar zenith angle	-
r_{cld}	Ratio based on cloudiness	-
θ_z	Solar zenith angle	radian
θ_c	Zenith angle of the edge from the centre of the CH bottom	radian
κ_d	Broadband flux extinction coefficient of ice for direct component	m^{-1}
κ_f	Broadband flux extinction coefficient of ice for diffuse component	m^{-1}
κ_{clr}	Broadband flux extinction coefficient of ice for clear sky	m^{-1}
κ_{cld}	Broadband flux extinction coefficient of ice for cloudy sky	m^{-1}
D_t	Depth of cryoconite hole	mm

570

Table 2: Descriptions of cryoconite holes (CH) and ice surface reflectance at the study sites in 2012, 2014, and 2017. CH depths and diameters were observed using a ruler.

Site (year)	Elevation (m a.s.l.)	DOY	Number of samples	Depth (mean ± SD mm)	Diameter (mean ± SD mm)	Ice surface reflectance (Observational date)
3 (2012)	672 m	186	30	38 ± 13	33 ± 10	No data
1 (2014)	247 m	186	31	141 ± 17	39 ± 19	0.68 ± 0.03 (DOY 176)
2 (2014)	441 m	186	31	186 ± 26	51 ± 24	0.57 ± 0.03 (DOY 176)
3 (2014)	672 m	205	50	86 ± 16	33 ± 16	0.40 ± 0.07 (DOY 203)
4 (2014)	772 m	205	50	110 ± 24	43 ± 19	0.41 ± 0.08 (DOY 203)
1 (2017)	247 m	189	20	168 ± 30	48 ± 20	0.56 ± 0.11 (DOY 211)
2 (2017)	441 m	189	20	149 ± 28	41 ± 20	0.42 ± 0.04 (DOY 211)
3 (2017)	672 m	197	20	111 ± 31	38 ± 17	0.24 ± 0.06 (DOY 211)

575

Table 3: Overview of the sensitivity tests. Changing ranges for each variable are assumed based on the field observations in this
580 **study.**

	ΔT_a (°C)	R_S component	D_0 (mm)	ϕ (mm)	α_i (-)	α_c (-)	κ_d ratio (times)	κ_f ratio (times)
Values for control experiment	3.92	Both Sd and Sf	185	50	0.57	0.1	1	1
Experiment ID	T_a-exp	R_S-exp	D_0-exp	ϕ-exp	α_i-exp	α_c-exp	κ_d-exp	κ_f-exp
Changing range	-3–+3*	Sd or Sf[+]	0–200	10–110	0.3–0.7	0.05–0.3	0.25–4.0	0.25–4.0

* change from the control experiment

[+] shortwave radiation assumed to be only direct or diffuse component
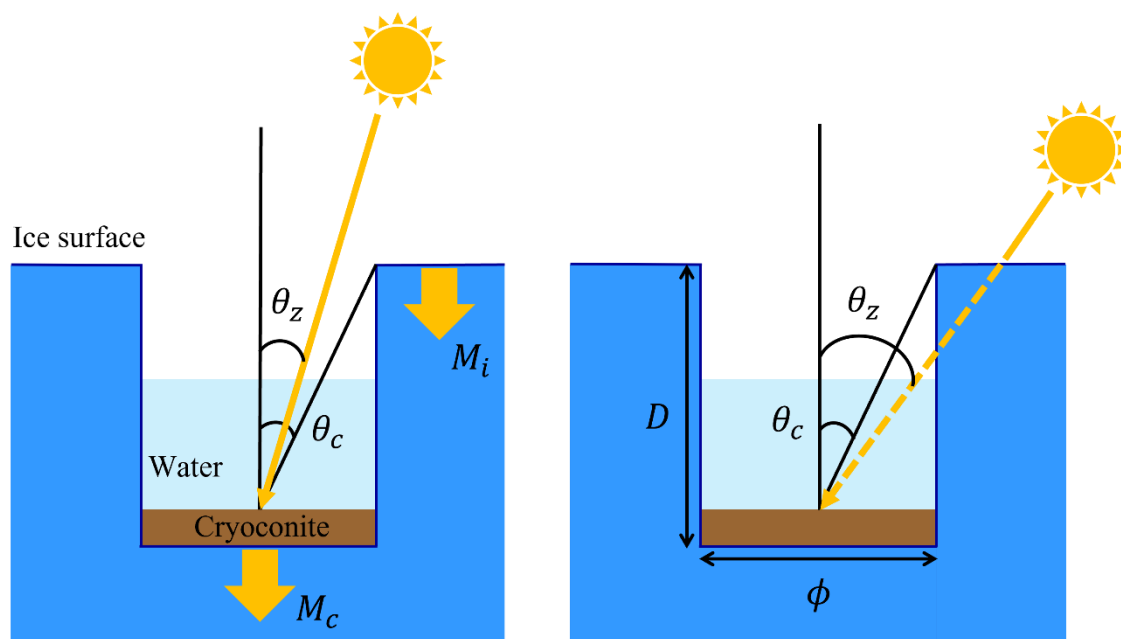
585 **Figure 1: Concept of the cryoconite hole model (CryHo). Heat balances at the surface and cryoconite hole bottom are independently calculated (left). Cryoconite hole (CH) geometry, with depth (D) and diameter (ϕ) being considered for distinguishing the components of shortwave radiation (right). Cryoconite thickness at the CH bottom is assumed to be zero in the model. The difference between the melt rate at the surface (M_i) and that at the CH bottom (M_c) changes the CH depth. The direct component of solar radiation can reach the CH bottom directly if the solar zenith angle θ_z is smaller than the zenith angle of the CH edge θ_c (left), while**
590 **it is transmitted through the ice if the solar zenith angle is greater than the zenith angle of the CH edge (right). The diffuse component of downward shortwave radiation is described in the method.**
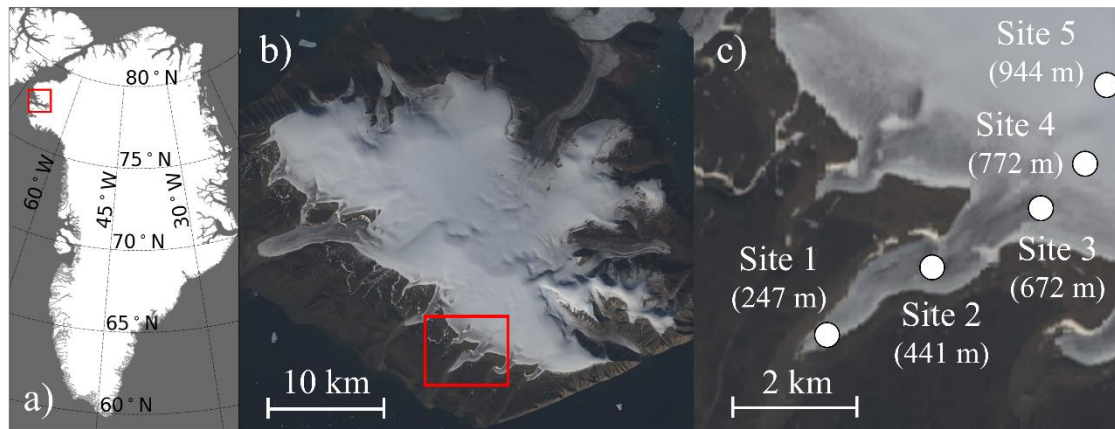
Figure 2: (a) Map of Greenland, (b) Qaanaaq ice cap in Northwest Greenland, and (c) study sites along the Qaanaaq Glacier. Panels b and c are true-colour composite images of Sentinel-2 taken on 24 July 2017. Red rectangles in panels a and b indicate the Qaanaaq area and Qaanaaq Glacier, respectively.
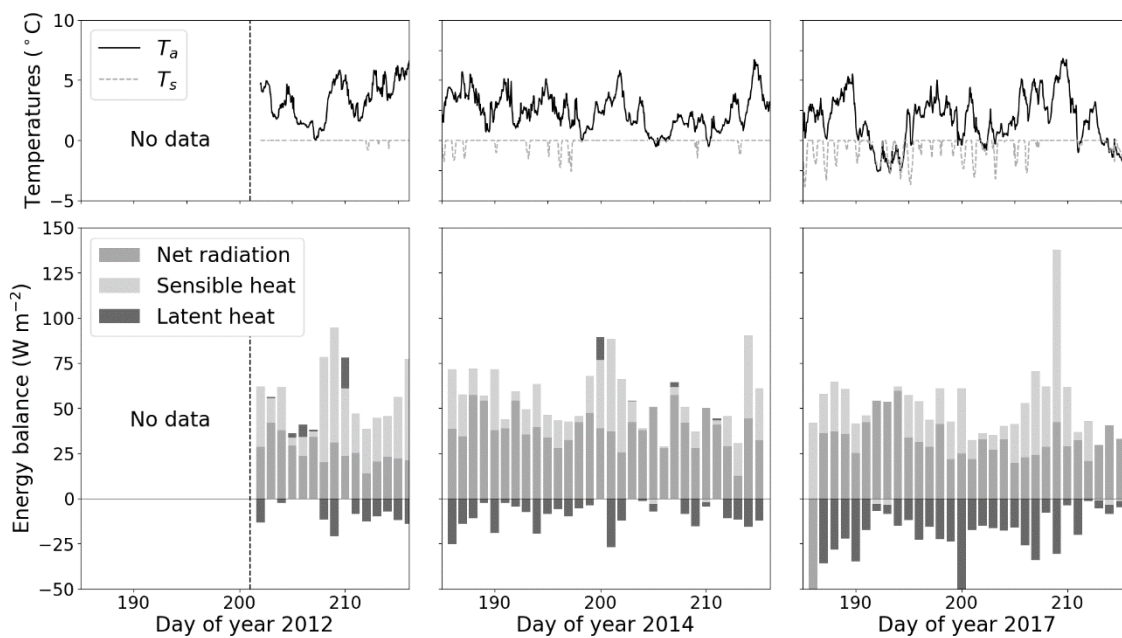
Figure 3: Hourly air and surface temperatures (T_a and T_s in the upper panels, respectively) and daily surface energy balance (lower panels) at the Sigma-B site (Site 5 in this study) on the Qaanaaq ice cap during the 2012, 2014, and 2017 summer seasons from left to right, respectively. T_s is calculated from the downward and upward longwave radiations. Daily surface energy balance is calculated with CryHo.
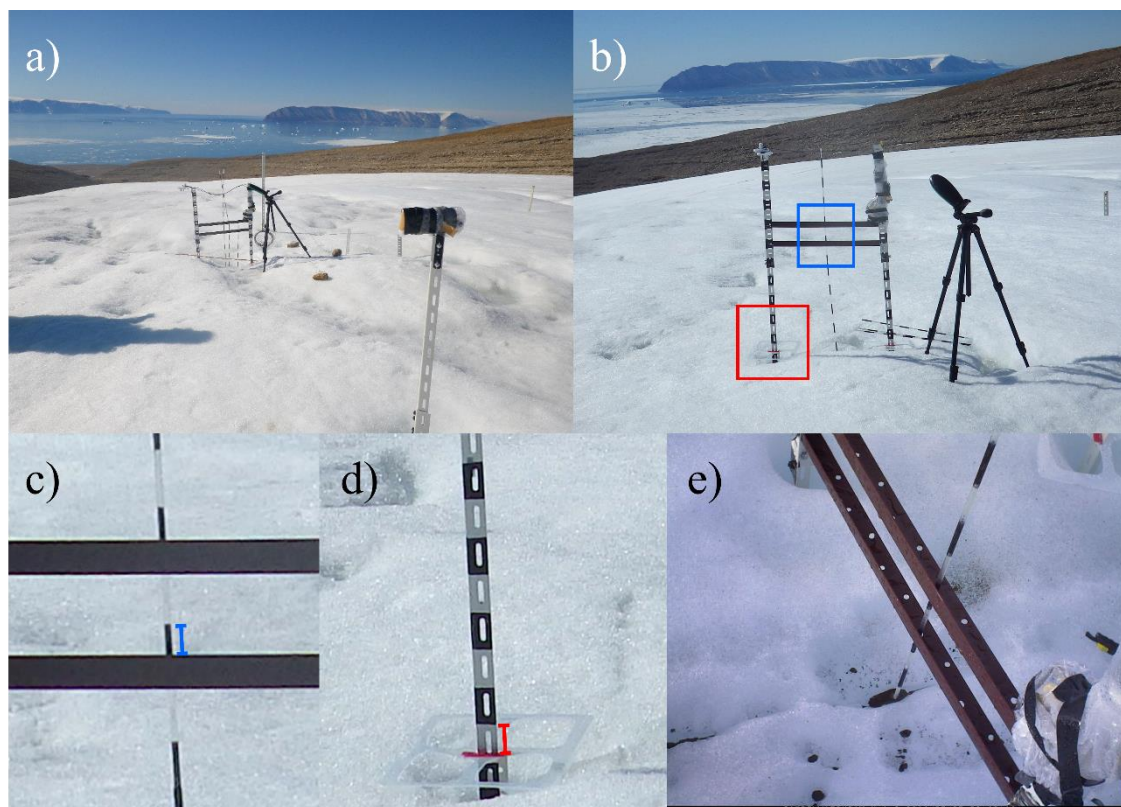
Figure 4: (a) Device for monitoring the cryoconite hole (CH) depth at Site 2, (b) sample image to quantify the CH depth, which was taken by the interval camera (PENTAX WG-10) on day of the year (DOY) 186 in 2014, (c) close-up of the image within the blue rectangle in panel b, (d) close-up of the image within the red rectangle in panel b, and (e) CH conditions monitored by the interval camera (GardenWatch Cam) on DOY 208 in 2014. Blue and red bars in panels c and d indicate measured lengths to estimate the vertical changes in CH bottom and ice surface, respectively. Because the ice surface was uneven, the ice surface level was inferred based on the red tape pasted on the clear plastic frame shown in panel d.

610
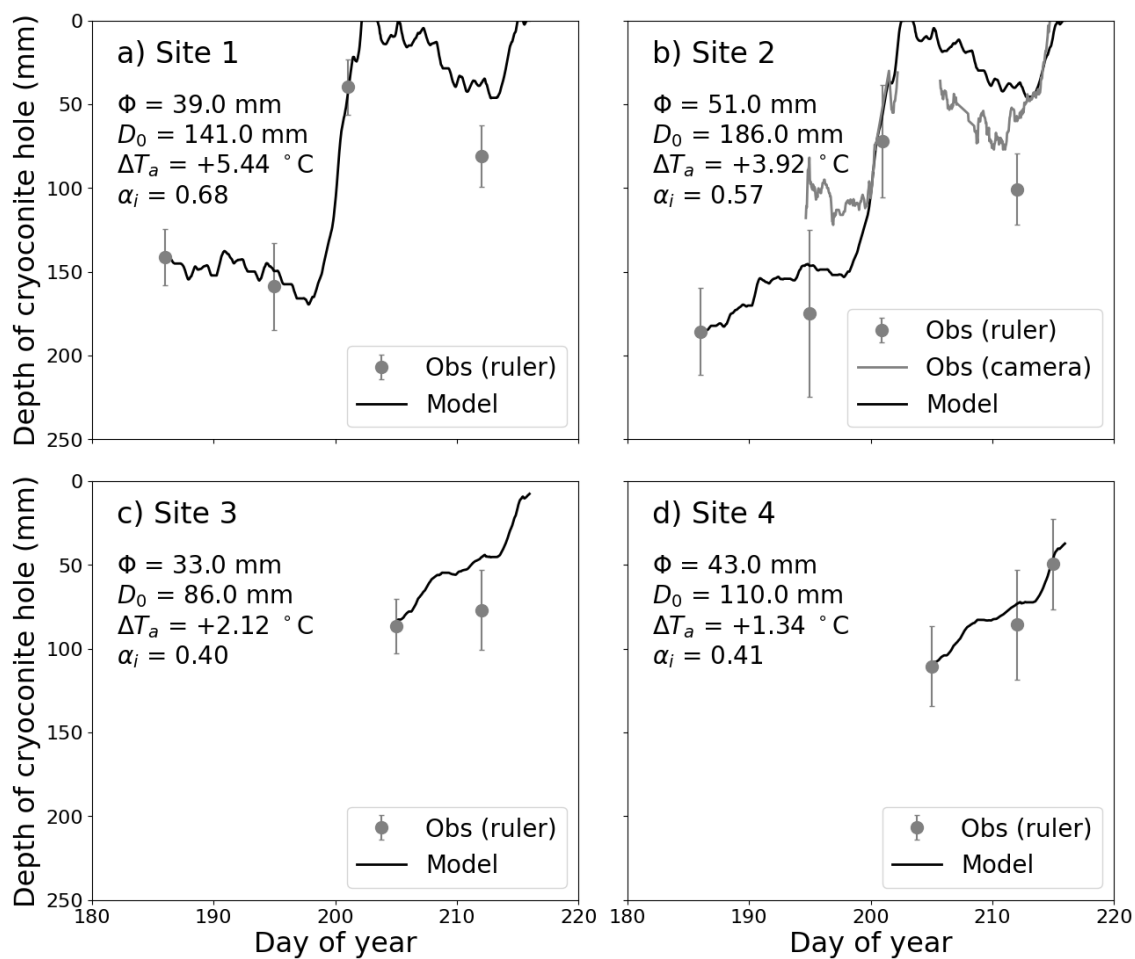
Figure 5: Temporal changes in cryoconite hole (CH) depth at (a) Site 1, (b) Site 2, (c) Site 3, and (d) Site 4 in 2014. The CH constants and air temperature correction are described in each panel. The missing grey solid line in panel b denotes the CH collapse period.
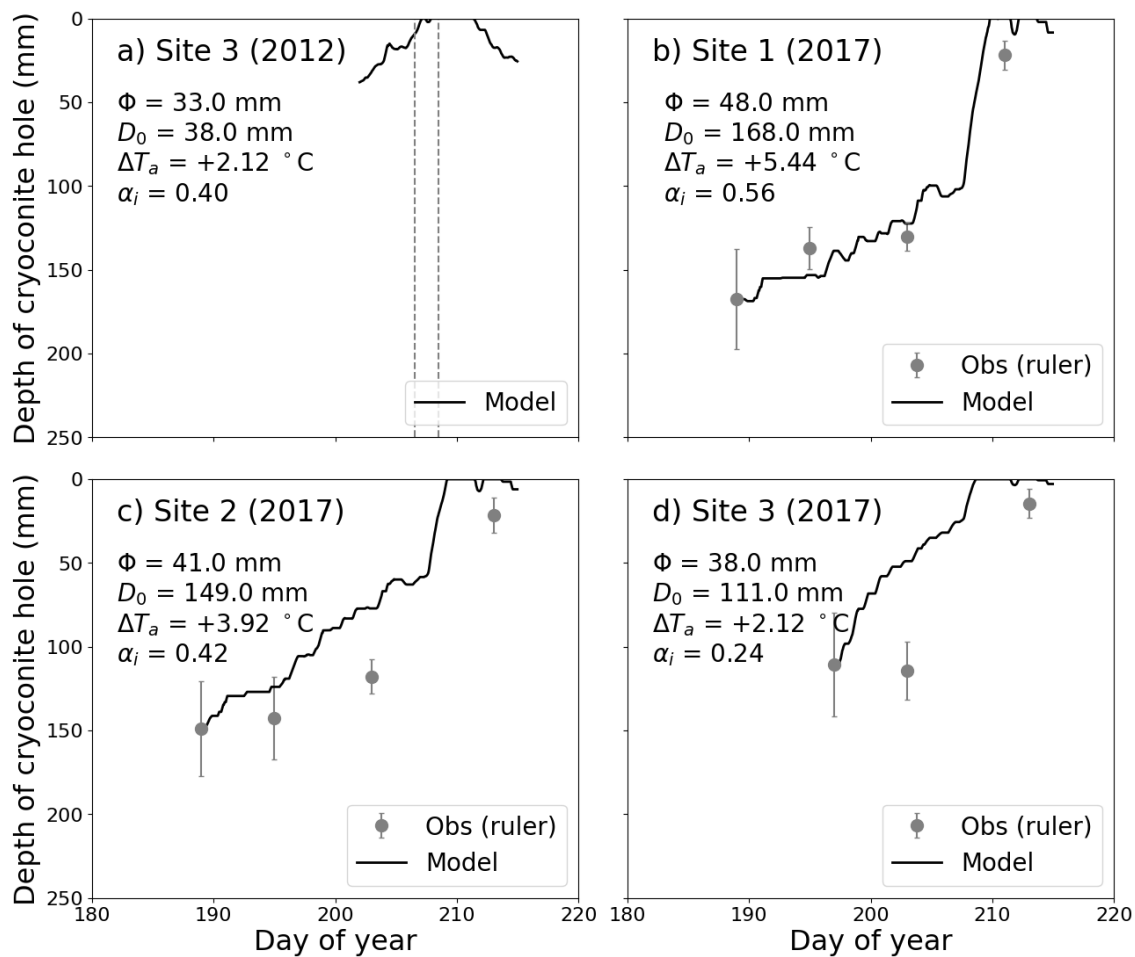
Figure 6: Temporal changes in cryoconite hole (CH) depth at (a) Site 3 in 2012, (b) Site 1 in 2017 (c) Site 2 in 2017, and (d) Site 3 in
620   **2017. The CH constants and air temperature correction are described in each panel. Grey dashed lines in the panel a indicate the**
collapse dates reported by Takeuchi et al. (2018).
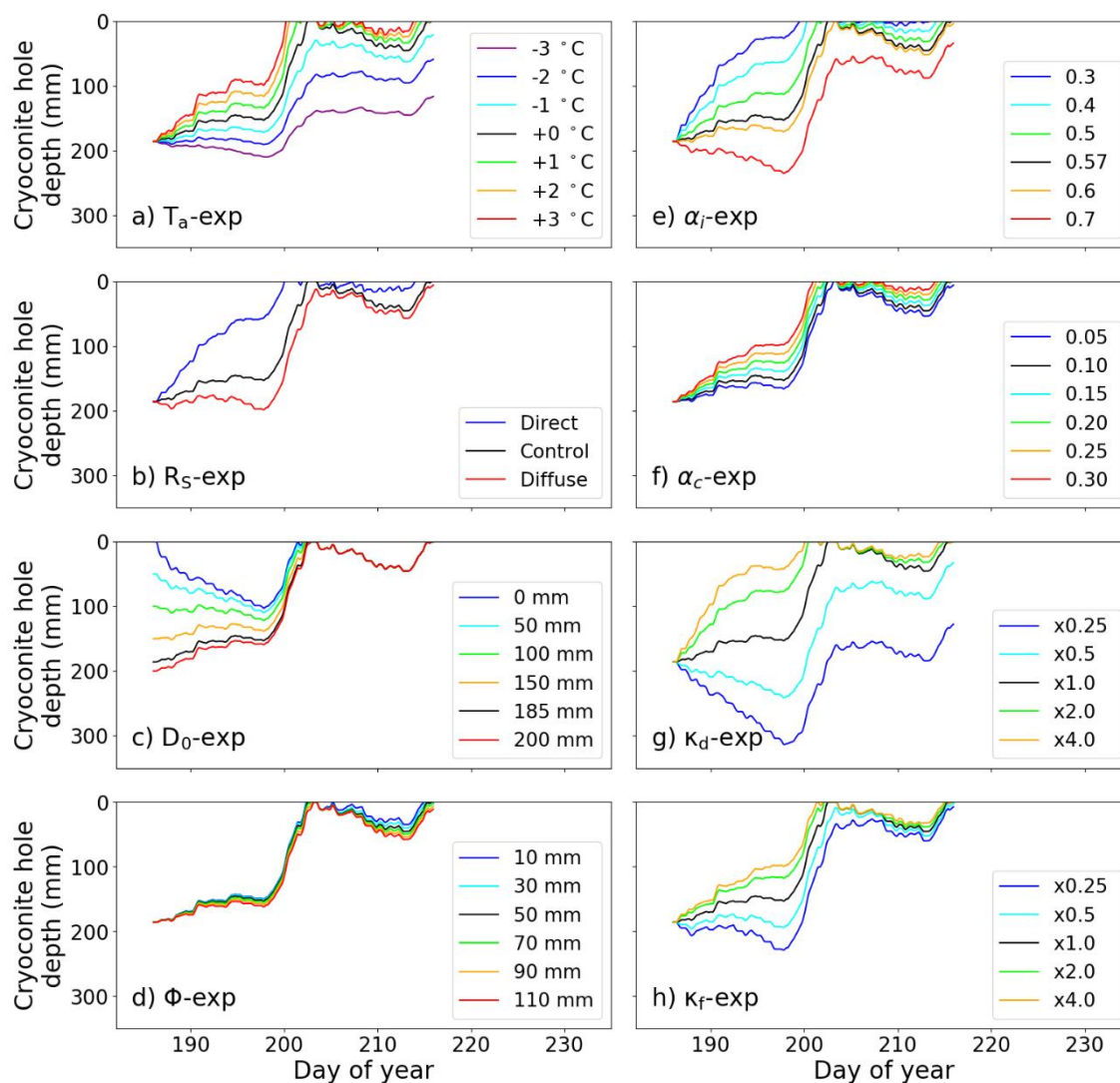
Figure 7: Sensitivity experiments of the temporal changes in cryoconite hole (CH) depth to model parameters and meteorological conditions at Site 2 in 2014. (a) Air temperature (T_a-exp), (b) shortwave radiation (R_S-exp), (c) initial CH depth (D_0-exp), (d) CH diameter (ϕ-exp), (e) ice surface albedo (α_i-exp), (f) cryoconite albedo (α_c-exp), and broadband flux extinction coefficient of ice for the (g) direct component (κ_d-exp) and (h) diffuse component (κ_f-exp). Black lines in each figure indicate the control experiment (Ctl-exp).

630
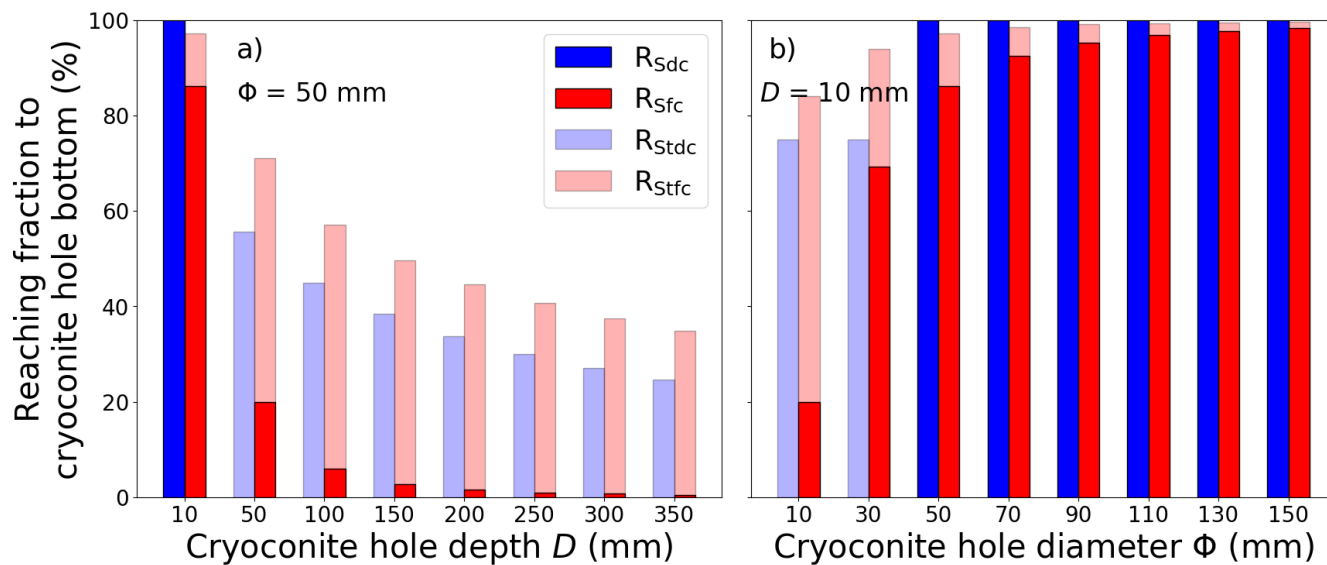
Figure 8: Sensitivity experiments of the cryoconite hole (CH) geometry on the direct and diffuse components of shortwave radiation reaching the CH bottom for (a) CH depth and (b) CH diameter. Dark blue and red bars in the figure indicate the direct and diffuse components of shortwave radiation, respectively. Light blue and red bars indicate the direct and diffuse components of shortwave
635 **radiation transmitted throughout ice, respectively. The vertical axis represents the fraction of direct and diffuse components against the incoming shortwave radiation at the ice surface (100 % at the ice surface). The ratios were derived from numerical simulations with different CH depth or CH diameter on day of the year (DOY) 172 in 2014. The meteorological conditions for the simulations were assumed to be those at 14:00 local time on the date used for Ctl-exp.**
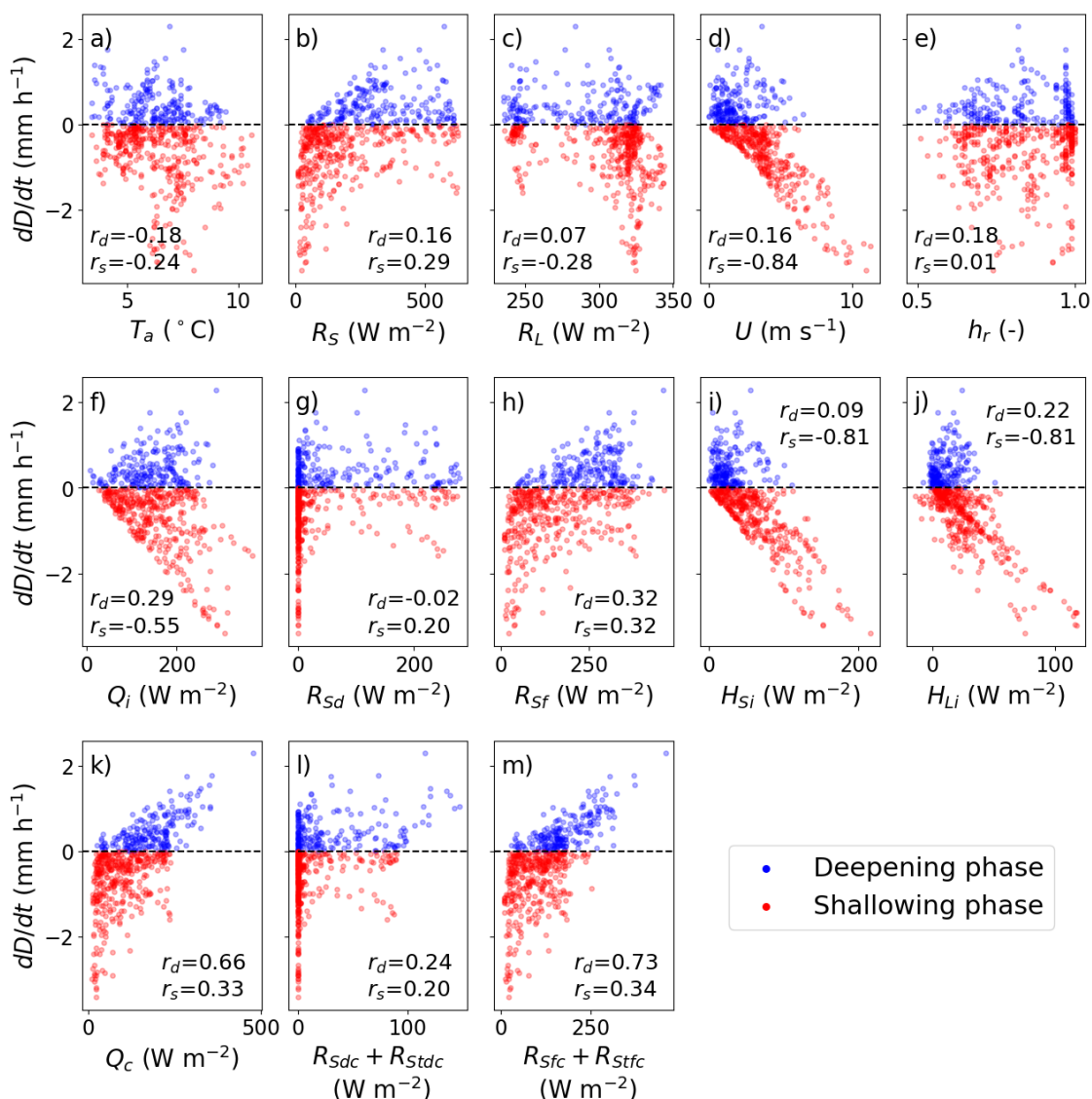
Figure 9: Relationships between the CH deepening or shallowing rates in the control experiment (dD/dt, mm h⁻¹). The upper (a–e), middle (f–j) and bottom (k–m) panels indicate the relationships between the CH deepening or shallowing rates and the input meteorological conditions, simulated heat properties at the ice surface, and simulated heat properties at the CH bottom, respectively. Blue and red marks indicate the CH deepening and shallowing, respectively. Variables in the horizontal axis are shown in Table 1.

640

645 **r_d and r_s in each panel indicate the correlation coefficients with CH deepening and shallowing rates, respectively. Note that T_a in the panel a is air temperature corrected for Site 2 where the control experiment was performed.**
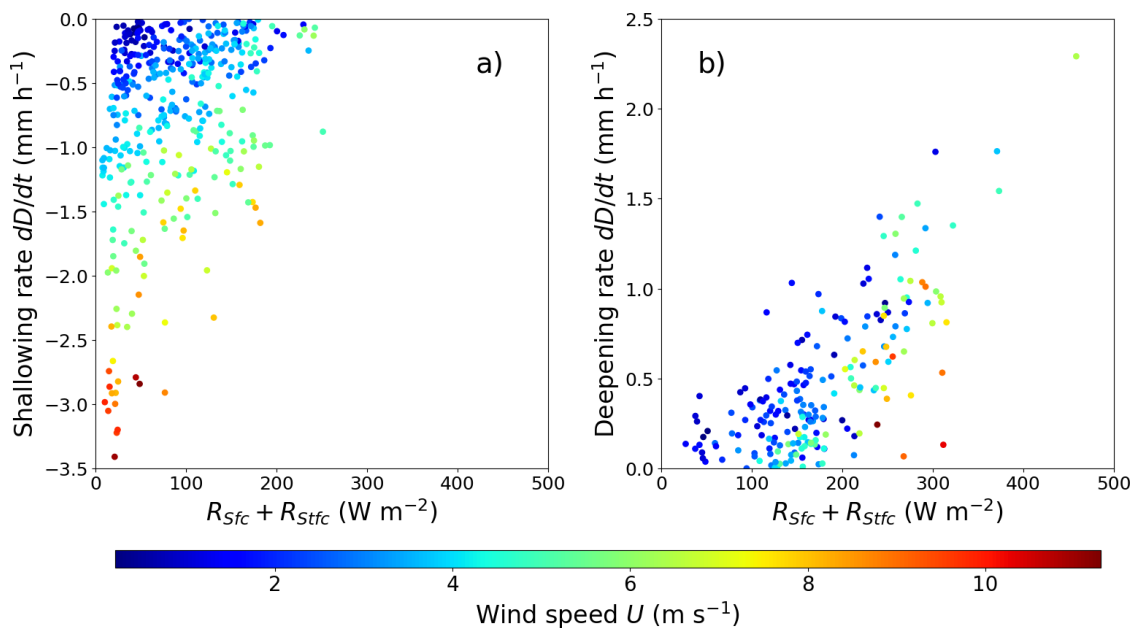
Figure 10: Relationships between the cryoconite hole (CH) (a) deepening or (b) shallowing rates and the diffuse component of downward shortwave radiation reaching the CH bottom and wind speed in the control experiment. The CH shallowing and deepening phases shown in Figure 9m are separated into panels a and b in this figure, respectively. The contour in the panels indicates the input wind speed for the control experiment.

650